

Accurate Detection of Demosaicing Regularity for Digital Image Forensics

Hong Cao, *Student Member, IEEE*, and Alex C. Kot, *Fellow, IEEE*

Abstract—In this paper, we propose a novel accurate detection framework of demosaicing regularity from different source images. The proposed framework first reversely classifies the demosaiced samples into several categories and then estimates the underlying demosaicing formulas for each category based on partial second-order derivative correlation models, which detect both the intrachannel and the cross-channel demosaicing correlation. An expectation-maximization reverse classification scheme is used to iteratively resolve the ambiguous demosaicing axes in order to best reveal the implicit grouping adopted by the underlying demosaicing algorithm. Comparison results based on syntactic images show that our proposed formulation significantly improves the accuracy of the regenerated demosaiced samples from the sensor samples for a large number of diversified demosaicing algorithms. By running sequential forward feature selection, our reduced feature sets used in conjunction with the probabilistic support vector machine classifier achieve superior performance in identifying 16 demosaicing algorithms in the presence of common camera postdemosaicing processing. When applied to real applications, including camera model and RAW-tool identification, our selected features achieve nearly perfect classification performances based on large sets of cropped image blocks.

Index Terms—Color filter array, digital still camera, demosaicing, image regularity, RAW tool, source identification.

I. INTRODUCTION

CAMERAS are regarded as trustworthy devices, and photos traditionally imply truth. Nowadays, digital photos have been widely used as historical records and as evidences of real occurrences in applications including journalistic reporting, police investigation, law enforcement, insurance, medical and dental examination, the military, museums, and consumer photography. While digital photos are conveniently used, their credibility has been severely challenged due to numerous fraudulent cases involving image forgeries, e.g., fake results on human stem-cell research [1]. Numerous low-cost yet powerful digital tools have enabled easy image creation, modification and distribution, which make image forgeries easier than ever. To restore the public trust in digital photos, passive image forensics has become a booming research area to mainly address photo authentication challenges, such as source identification, tampering discovery, and steganalysis. As

suggested in [2], forensic software is urgently needed for scientific journal editors to detect signs of deliberate image tweaks. Very often, image forensics needs to detect common tampering artifacts or inconsistencies of certain image regularities. Since passive image forensics does not rely on hiding information, which usually requires cooperative sources and compatible end-to-end protocols, it has a brighter application prospect than active forensics.

Recently, passive forensics has been studied for digital images acquired by various digital still cameras (DSCs) and scanners. For DSCs, previous works have mainly detected the following intrinsic image regularities:

- *optical regularities*: illumination, lens distortion [10], and chromatic aberration;
- *sensor imperfections*: sensor noise [11], [17], [20], dust pattern [15], and camera response function [16];
- *processing regularities*: demosaicing [3]–[7], [18], [19] white balancing, gamma correction, and JPEG compression;
- *statistical regularities*: image quality metrics [8], wavelet statistics [12], and binary similarity metrics.

The different regularities are associated with different origins, and their detections are useful in various forensic tasks. For instance, the work in [11], [17], and [20] extracts photoresponse nonuniformity (PRNU) sensor noises for individual camera identification and tampering detection. The work in [7], [18], and [19] estimates the demosaicing parameters for nonintrusive component forensic analysis on different camera models. Reference [14] fuses several types of statistical image regularities and applies a feature selection technique to blindly identify cellular camera models from their output low-resolution images. The forensic performances depend on both the image regularity types and the appropriateness of the detection methods. It is also pointed out in [9] and [13] that comprehensive forensic analysis should be based on a suite of forensic tools that examine different image properties. In general, a forensic system based on one type of regularity may be attacked with ease by a sophisticated attacker, while covering up all tampering artifacts and restoring all image regularities into a tampered photo is believed to be very difficult.

In this paper, we consider accurate detection of demosaicing regularity, an important processing regularity associated with single-chip camera processing [Fig. 1(a)]. This is motivated by the fact that 2/3 of color samples of a common photo are reconstructed by a demosaicing technique consisting of only a few formulas, and this large population of reconstructed samples provides a good basis of reliable statistical characterization of the applied demosaicing technique. In this paper, we aim to accurately estimate the demosaicing formulas for diversified demosaicing algorithms. Our proposed framework employs

Manuscript received February 18, 2009; revised September 13, 2009. First published October 09, 2009; current version published November 18, 2009. The associate editor coordinating the review of this manuscript and approving it for publication was Dr. Min Wu.

The authors are with the School of Electrical and Electronic Engineering, Nanyang Technological University, Singapore 640732, Singapore (e-mail: hcao@ntu.edu.sg; eackot@ntu.edu.sg).

Color versions of one or more of the figures in this paper are available online at <http://ieeexplore.ieee.org>.

Digital Object Identifier 10.1109/TIFS.2009.2033749

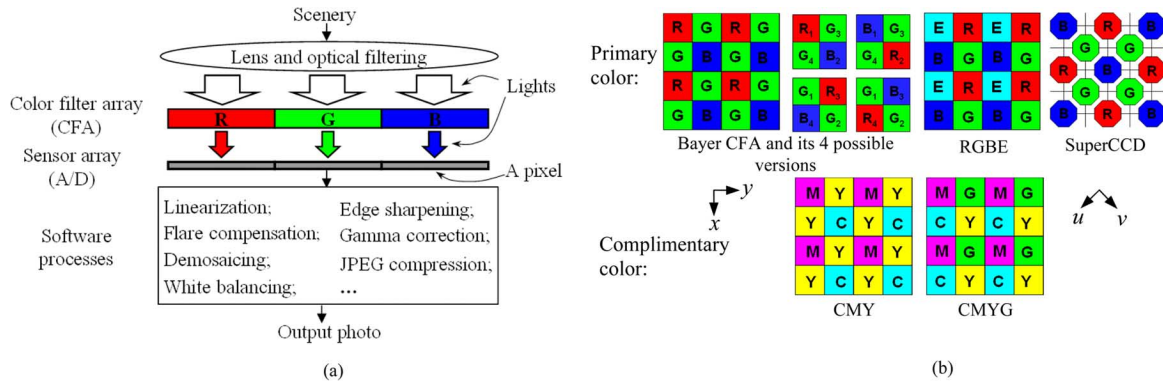


Fig. 1. (a) Typical camera processing pipeline for a single-chip digital still camera [25]. (b) Common color filter array patterns.

a partial second-order image derivative correlation model, which detects both the intrachannel and the cross-channel demosaicing correlation. A reverse classification scheme is incorporated to precisely classify the demosaiced samples into small categories, which best reveal the original demosaicing grouping. Compared with an existing method, our estimated demosaicing formulas regenerate the demosaiced samples from the sensor samples with significantly improved accuracy. Our reduced set of demosaicing features also performs significantly better in identification of 16 demosaicing algorithms in the presence of common camera postdemosaicing processes. For real applications, including camera and RAW-tool identification, large-scale tests show that our proposed features achieve nearly perfect identification performances based on the cropped image blocks.

This paper is organized as follows. In Section II, we briefly describe the major differences of existing demosaicing algorithms and discuss the existing detection methods of demosaicing regularity. Section III derives the second-order derivative formula based on one-dimensional (1-D) periodical lattice and introduces the partial derivative correlation model. With an assumption that Bayer color filter array (CFA) is used, Section IV details the proposed detection framework based on partial derivative correlation model. Section V experimentally compares the proposed detection framework with two existing detection methods based on syntactic images. With features selected using sequential forward floating search algorithm, Section VI demonstrates the efficacy of proposed demosaicing features in identification of commercial DSCs and RAW-tools. Section VII concludes this paper and indicates future work.

II. DEMOSAICING AND EXISTING DETECTION METHODS

Color filtering and demosaicing are common processes in commercial DSCs to economically produce color. As shown in Fig. 1(a), the color filtering with a CFA allows one specific color to be captured at each pixel. Consequently, only one color is present at each pixel in the resultant RAW image, and the missing color samples are reconstructed through demosaicing. The common CFA patterns in Fig. 1(b) are typically arranged in a mosaic manner on 2×2 periodical lattices.

As a key process that determines the fidelity of a color photo, demosaicing has been extensively studied [26]–[28]. We summarize the major differences with regard to color filtering and demosaicing.

- *CFA pattern*: The most commonly used is Bayer CFA [Fig. 1(b)] [28].
- *Grouping*: The missing color samples are typically grouped before an appropriate demosaicing formula is applied for each group. The grouping can be edge-adaptive or nonadaptive. For edge-adaptive algorithms, the decision criteria differ significantly for distribution of the samples to different edge groups.
- *Reconstructive filtering*: The reconstruction is commonly performed in the color-difference domain. Other possible domains include the intrachannel domain and the color-hue domain. The low-pass reconstruction filters differ significantly in their kernel parameters and sizes.
- *Refinement and enhancement*: As an optional step, the refinement is commonly iterated in updating the green channel and then the red and blue channels. The updating formulas also differ in their parameters.

Several previous forensic works have characterized the demosaicing regularity for both source identification and tampering detection. The work in [3] and [4] uses an expectation-maximization (EM) technique to compute a set of weights for classification of several demosaicing algorithms and for identification of cameras. Reference [5] extends the EM technique by using both the derived EM weights and the average second-order derivative spectrum as features for camera identification. In [6], quadratic pixel correlation coefficients are proposed as demosaicing features for camera identification. Though reasonable accuracies for identification of three to four commercial cameras are reported, these methods are not practical due to an overly simplified implicit assumption, i.e., each pixel is equally correlated with its neighboring pixels in a color channel. The work in [7] introduces several new concepts.

- 1) Detection of the CFA pattern.
- 2) Heuristic division of the image into three regions—the horizontal edges, the vertical edges, and the smooth region—with an assumption that the demosaicing formula for each region is similar.
- 3) Each demosaiced sample is written as a weighted average of its neighboring sensor samples in the same color channel, and the optimal weights are solved as a total least squares solution [24].

Inspired by the new concepts, we also note this detection method has two major drawbacks: 1) the incapability of capturing the cross-color channel correlations caused by demosaicing and 2) the roughness of the heuristic division, which

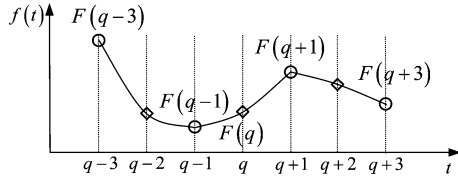


Fig. 2. A 1-D array of periodical color samples extracted from one color channel of a demosaiced image, where “o”s are sensor samples and “◇”s are demosaiced samples. $F(q)$ is demosaiced along the t -axis.

largely depends on an empirical threshold and cannot accurately reveal the true varying demosaicing grouping for diversified demosaicing algorithms.

In this paper, with the assumption that various demosaicing algorithms reconstruct smooth samples from neighboring sensor samples, we compute in Section III the partial second-order derivative of a demosaiced sample. This provides rich information of the applied demosaicing formula and, at the same time, it does not contain the local DC component within a color channel. By proposing a partial derivative correlation model, our estimation of the underlying demosaicing formulas is naturally extended across the boundaries of color channels. In addition, a proposed reverse classification scheme in Section IV precisely classifies samples demosaiced by the same formula into the same category, which minimizes the detection variations due to classification errors. Both the partial derivative correlation model and the reverse classification improve the detection accuracy by suppressing content dependant estimation variations for color images undergoing the same demosaicing process. Three types of features computed from 16 categories of demosaiced samples comprehensively represent the regularity introduced by demosaicing. Since forensic challenges are commonly formulated as pattern classification problems, by enhancing the detection accuracy and improving comprehensiveness of the feature description, we suppress the within-class feature variations and enlarge the between-class separation. Consequently, this leads to superior forensic performances, especially when our proposed method is compared with several existing demosaicing detection methods in Section V.

III. PARTIAL DERIVATIVE CORRELATION MODEL

A. Image Derivative on 1-D Periodical Lattice

Since common CFAs reside on a 2×2 periodical lattice as in Fig. 1(b), and demosaicing is frequently carried out along one axis, we first derive the second-order derivative formula based on a 1-D periodical mosaic lattice in Fig. 2, where $\{F(n), n = 1, 2, \dots\}$ can be viewed as discrete samples from a smooth continuous function $f(t)$ at equal sampling intervals. The indexes $\{\dots, q-1, q+1, \dots\}$ and $\{\dots, q-2, q, q+2, \dots\}$ are, respectively, associated with the sensor samples and the demosaiced samples.

Suppose $F(q)$ is demosaiced along the t -axis; it is reasonable to assume $f(t)$ is smooth at $t = q$ such that both the left and the right derivatives of $f(t)$ are continuous at $t = q$, and Taylor series expansions are applicable below

$$F(q+d) = F(q) + \frac{f^1(q)}{1!}d + \frac{f^2(q)}{2!}d^2 + \frac{f^3(q)}{3!}d^3 + \dots \quad (1)$$

With the second-order approximation on the Taylor series expansions, we consider below a small neighborhood including the nearest sensor samples $F(q-1)$ and $F(q+1)$

$$\begin{cases} F(q+1) = F(q) + f^1(q) + f^2(q)/2 \\ F(q-1) = F(q) - f^1(q) + f^2(q)/2. \end{cases} \quad (2)$$

From (2)

$$f^2(q) = F(q-1) + F(q+1) - 2F(q). \quad (3)$$

Or, equivalently

$$F(q) = \alpha^T \gamma - \beta f^2(q) \quad (4)$$

where $\alpha = [0.5 \ 0.5]^T$, $\gamma = [F(q-1) \ F(q+1)]^T$ and $\beta = 0.5$. Since $F(q-1)$ and $F(q+1)$ are known sensor samples, $F(q)$ is linearly correlated with and directly computable from $f^2(q)$, its second-order derivative along the t -axis. Therefore, various demosaicing algorithms that estimate $F(q)$ along the t axis are equivalent to estimating $f^2(q)$ first, followed by applying a known linear transformation in (4).

The above formulation can be extended to a higher order approximation by considering a larger neighborhood of sensor samples. For instance, with the fourth-order approximation, we can further include sensor samples $F(q-3)$ and $F(q+3)$ to form a set of equations in a similar manner to those in (2). Through elimination process, a similar second-order derivative formula to (3) can be derived. In such a case, (4) still holds with α , γ , and β changed correspondingly.

Since only second-order derivatives are used in our formulation, in what follows, we use “derivative” to represent “second-order derivative.”

B. Derivative-Based Demosaicing Model

To detect the image regularity associated with demosaicing, it is important to have a generalized model to represent the demosaicing processes so that different demosaicing formulas differ only in some free model parameters. Below, we propose a partial derivative correlation model for such a purpose.

To facilitate the discussion, we let $\mathbf{D} = \{D_{ijc}\}$ represent a three-dimensional array of the demosaiced image of size $H \times W \times K$, where H and W are the height and width of the image, respectively, and $K = 3$ denotes the number of color channels. c indicates the red, green, and blue channels for a Bayer CFA. Suppose the CFA pattern is known; we can sample the two-dimensional RAW image $\mathbf{S} = \{S_{ij}\}$ from \mathbf{D} accordingly. As an example, \mathbf{D} and \mathbf{S} for the first Bayer CFA pattern in Fig. 1(b) can be represented as

$$\mathbf{D} = \{D_{ijc}\} = \begin{pmatrix} \{r, G, B\}_{11} & \{R, g, B\}_{12} & \dots \\ \{R, g, B\}_{21} & \{R, G, b\}_{ij} & \\ \vdots & & \ddots \end{pmatrix}$$

$$\mathbf{S} = \{S_{ij}\} = \begin{pmatrix} r_{11} & g_{12} & \dots \\ g_{21} & b_{ij} & \\ \vdots & & \ddots \end{pmatrix} \quad (5)$$

where capital letters R, G , and B denote the demosaiced samples in the red, green, and blue color channels, respectively, and lowercase letters r, g , and b denote the sensor samples.

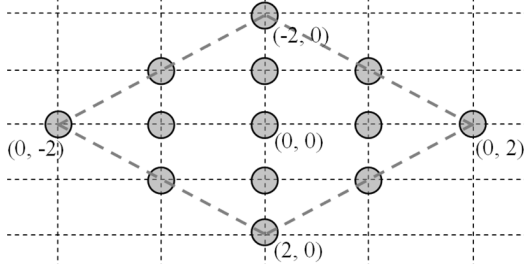


Fig. 3. Diamond weight pattern.

Suppose a sample D_{ijc} is demosaiced along the t -axis, where $t \in \{x, y, u, v\}$ is as depicted in Fig. 1(b) and, since from (4), demosaicing D_{ijc} along the t axis is equivalent to estimation of its partial derivative $D_{ijc}^{(t)}$ along the t -axis, we can write a general demosaicing equation as

$$D_{ijc}^{(t)} = \sum_{\forall(p,q) \in \Omega} w_{pq}^{(t)} S_{i+p,j+q}^{(t)} + e_{ijc}^{(t)} \quad (6)$$

where $S_{ij}^{(t)}$ denotes a supporting RAW partial derivative computed from \mathbf{S} along the t -axis; $\{w_{pq}^{(t)}\}$ are weights of the supporting derivatives $\{S_{ij}^{(t)}\}$, which represent the formula used to demosaic D_{ijc} ; $e_{ijc}^{(t)}$ is the corresponding estimation error; and $\Omega = \{(p, q), \text{ where } p^2 + q^2 \leq 4\}$ defines a diamond weight pattern, as shown in Fig. 3. Based on the second-order approximation, we use the derived derivative formula in (3) to compute the partial derivatives. For instance, the x axis derivatives are

$$\begin{aligned} D_{ijc}^{(x)} &= D_{i-1,jc} + D_{i+1,jc} - 2D_{ijc} \\ S_{ij}^{(x)} &= S_{i-2,j} + S_{i+2,j} - 2S_{ij}. \end{aligned} \quad (7)$$

Note that \mathbf{S} contains sensor samples of all three color channels; and samples $S_{i-2,j}$, S_{ij} and $S_{i+2,j}$ belong to the same color channel due to the 2×2 periodicity of the commonly used CFAs in Fig. 1(b). This periodicity of the CFA also applies for other axes, including y , u , and v . The partial derivative formulas along the y -, u -, and v -axes can be written similar to (7).

We also note that for a number of demosaicing algorithms, one color plane c_l with rich luminance information (green for a Bayer CFA) is reconstructed first. The reconstruction of another color plane c_c with rich chrominance information (red or blue for a Bayer CFA), is based on both the fully populated color plane c_l and the RAW \mathbf{S} . To cater for such cases, we modify the demosaicing equation in (6) accordingly for a demosaiced sample D_{ijc_c} in the c_c color plane as

$$\begin{aligned} D_{ijc_c}^{(t)} &= \sum_{\forall(p,q) \in \Omega} w_{pq}^{(t)} S_{i+p,j+q}^{(t)} \\ &+ \sum_{\forall(p,q) \in \Omega} \mu_{pq}^{(t)} D_{i+p,j+q,c_l}^{(t)} + e_{ijc_c}^{(t)} \end{aligned} \quad (8)$$

where $\{\mu_{pq}^{(t)}\}$ are weights of the supporting derivatives $\{D_{ijc_l}^{(t)}\}$ along the t -axis.

Since the supporting derivatives $\{S_{ij}^{(t)}\}$ are computed from the sensor samples of all 3 color channels, our correlation models in (6) and (8) simultaneously take into account both the cross- and the intra-channel correlation. This is important

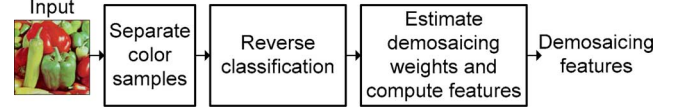


Fig. 4. Overview of the proposed demosaicing detection framework.

as the state-of-art demosaicing algorithms often employ color difference or hue domains for demosaicing and this inevitably introduces strong cross-channel correlation. The main advantage of using the partial derivative correlation models is that these derivatives do not contain any local DC component of the respective color channel, which allows estimation of the underlying demosaicing weights, being naturally extended across the boundary of different color channels. Comparatively, the conventional pixel-based correlation model can be hardly extended across the boundary of color channels, as the local DC levels in all three color channels are highly scenery dependant and generally unequal. By removing the local DC components, the derivative-based formulation focus on the correlation caused by demosaicing, and the estimation variations caused by different image sceneries are largely suppressed.

IV. PROPOSED DETECTION FRAMEWORK

Fig. 4 shows an overview of the proposed detection framework based on the partial derivative correlation model. Since Bayer CFA has been dominantly used in commercial DSCs [28], we first separate the sensor samples from demosaiced samples according to a Bayer CFA. Then a reverse classification scheme exclusively partitions all demosaiced samples into 16 categories. An expectation-maximization reverse classification (EMRC) algorithm is employed to resolve the ambiguous demosaicing axes. After the 16 categories are formed, the partial derivative correlation models are used to form a set of linear demosaicing equations, and the weights are estimated as a regularized least square solution. Three types of demosaicing features are computed from the 16 categories for image forensic applications. In the following section, we elaborate the steps in detail.

A. Reverse Classification to Estimate Demosaicing Weights

After separating the sensor samples \mathbf{S} and identifying the demosaiced samples from a given demosaiced image \mathbf{D} according to a Bayer CFA, we perform reverse classification to exclusively classify all demosaiced samples into a number of categories so that each category of demosaiced samples was reconstructed by the same or very similar formulas. The goal of the reverse classification is therefore to best recover the implicit grouping adopted by the underlying demosaicing algorithm. Precise reverse classification is a prerequisite to enable accurate estimation of the demosaicing formulas.

As shown in Fig. 5, our proposed reverse classification is implemented in two levels. In the first level, we divide the demosaiced samples according to their color channel and the relative positions in the 2×2 periodical CFA lattice. As a result, we form eight first-level categories, including two green categories and three each from the red and blue channels. In the second level, we first determine the possible demosaicing axes for each first-level category and further partition the first-level categories according to their possible demosaicing axes. As the first-level

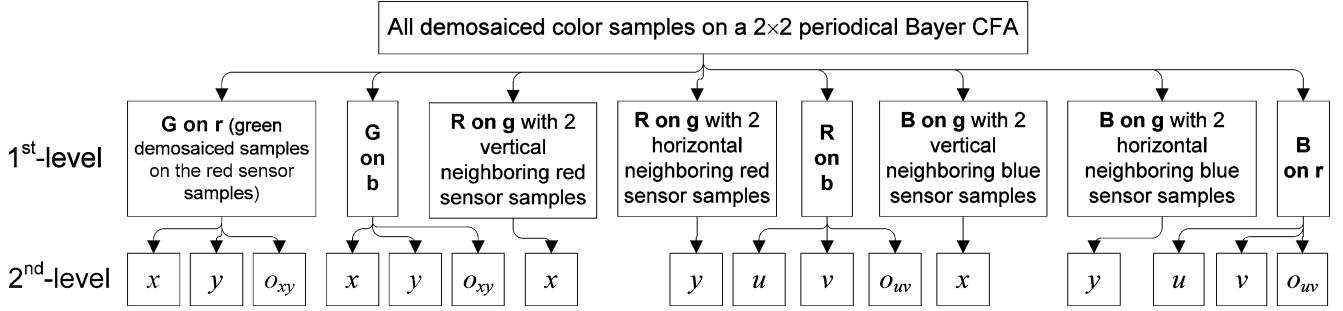


Fig. 5. Two-level reverse classification of the demosaiced samples for Bayer CFA into 16 categories with the demosaicing axes indicated.

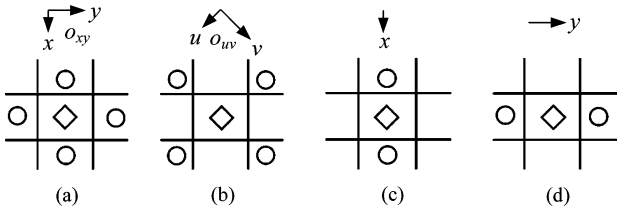


Fig. 6. Four patterns of nearest sensor samples for Bayer CFA, (“o”: sensor samples; “◇”: demosaiced samples); For green channel (a) four direct neighbors and for red and blue channels (b) four corner neighbors. (c) Two vertical neighbors and (d) two horizontal neighbors.

reverse classification is straightforward, below we focus on the second level.

For each of the eight first-level categories, the possible demosaicing axes are determined by examining the pattern of nearest surrounding sensor samples in the same color channel. Fig. 6 shows four possible patterns for Bayer CFA. For patterns (a) and (b), ambiguity arises as demosaicing can be conveniently carried out along either one of the two suggested axes or omnidirectionally, i.e., as an average of both axes. To resolve this ambiguity, we further partition such a first-level category into three second-level categories according to the three demosaicing axes by using an EMRC algorithm below. The goal of this EMRC algorithm is to jointly assign each sample to its most appropriate demosaicing axes and, at the same time, to estimate the corresponding demosaicing formulas.

We first consider the green-channel estimation and let $\{z_n\}$ for $1 \leq n \leq N$ denote a first-level green category, where N is $\lfloor H \times W/4 \rfloor$. The demosaiced samples $\{z_n\}$ are reorganized based on a single index n . This category is associated with the pattern in Fig. 6(a), and the possible demosaicing axes are x, y , and o_{xy} , i.e., average of the x - and y -axes. Let $\{z_n^{(1)}\}, \{z_n^{(2)}\}$ and $\{z_n^{(3)} = (z_n^{(1)} + z_n^{(2)})/2\}$ denote the corresponding x - and y axis derivatives and the average derivatives, respectively. For each sample z_n and each axis $t \in \{1, 2, 3\}$, we follow (6) to get

$$e_n^{(t)} = z_n^{(t)} - \mathbf{w}^{(t)T} \mathbf{s}_n^{(t)} \quad (9)$$

where $\mathbf{w}^{(t)}$ is a vector of the weights for the t th axis, $\mathbf{s}_n^{(t)}$ is a vector of the corresponding supporting RAW derivatives, and $e_n^{(t)}$ denotes the estimation error. The vectors $\mathbf{w}^{(t)}$ and $\mathbf{s}_n^{(t)}$ are formed by realigning all elements in the diamond weight pattern defined in Fig. 3 row by row into single-column vectors. For the o_{xy} -axis, $\mathbf{s}_n^{(3)}$ contains both the x - and y axis supporting derivatives.

Since the demosaicing weights $\mathbf{w}^{(t)}$ are unknown, directly assigning the most appropriate demosaicing axis for each sample z_n is impossible. Therefore, the proposed EMRC algorithm iteratively minimizes

$$J = \sqrt{\frac{1}{N} \sum_{n=1}^N \sum_{t=1}^3 v_n^{(t)} \left(z_n^{(t)} - \mathbf{w}^{(t)T} \mathbf{s}_n^{(t)} \right)^2} \quad (10)$$

where $v_n^{(t)} \in \{0, 1\}$ is the assignment indicator and $v_n^{(t)} = 1$ indicates that z_n is exclusively assigned to the t th-axis.

The weights for $\mathbf{w}^{(t)}$ are initially set to zero. In the *expectation step*, we update

$$v_n^{(t)} = \begin{cases} 1, & \text{if } t = \arg \min \left(\left| z_n^{(t)} - \mathbf{s}_n^{(t)T} \mathbf{w}^{(t)} \right| \right) \\ 0, & \text{otherwise} \end{cases} \quad (11)$$

for $n = 1, \dots, N$, while $\mathbf{w}^{(t)}$ is fixed.

In the *maximization step*, we fix $v_n^{(t)}$ and compute $\mathbf{w}^{(t)}$ as a regularized least squares solution [24] below

$$\min(\|\mathbf{Q}^{(t)} \mathbf{w}^{(t)} - \mathbf{z}^{(t)}\|^2 + \lambda \|\mathbf{w}^{(t)}\|^2) \Rightarrow \mathbf{w}^{(t)} = \mathbf{Q}^{(t)\dagger} \mathbf{z}^{(t)} \quad (12)$$

for $t = 1, 2$, and 3, where

$$\mathbf{Q}^{(t)} = \begin{bmatrix} v_1^{(t)} \mathbf{s}_1^{(t)T} \\ \vdots \\ v_N^{(t)} \mathbf{s}_N^{(t)T} \end{bmatrix}, \quad \mathbf{z}^{(t)} = \begin{bmatrix} v_1^{(t)} z_1^{(t)} \\ \vdots \\ v_N^{(t)} z_N^{(t)} \end{bmatrix},$$

$$\mathbf{Q}^{(t)\dagger} = \left(\mathbf{Q}^{(t)T} \mathbf{Q}^{(t)} + \lambda \mathbf{I} \right)^{-1} \mathbf{Q}^{(t)}.$$

$\|\cdot\|$ denotes Frobenius norm and λ is a small regularization constant that prevents overfitting and improves stability of the solutions especially under ill conditions. \mathbf{I} denotes an identity matrix. Since $\mathbf{w}^{(t)} = 0$ is also a valid solution but (12) hardly returns such a special solution, we set $\mathbf{w}^{(t)} = 0$ if $\|\mathbf{z}^{(t)}\| \leq \|\mathbf{Q}^{(t)} \mathbf{w}^{(t)} - \mathbf{z}^{(t)}\|$.

The above expectation and maximization steps are repeated until the following stabilization condition is met:

$$J^{(i-1)} - J^{(i)} < T_h \quad (13)$$

where i denotes the current iteration number and T_h is a small experimentally determined constant. Both the expectation and maximization steps are designed to reduce J , which is sharply reduced at the few initial iterations and gradually stabilized to a low level. T_h is chosen to speed up the iteration process for the EMRC algorithm. By setting $T_h = 0$, more iterations are

needed. Experimentally, with a small T_h in the range of [0.001 0.005], the required number of iterations drops significantly. As the outcomes of the EMRC algorithm, the true grouping employed by the underlying demosaicing technique can be largely recovered and the weights $\mathbf{w}^{(t)}$ representing the underlying demosaicing formulas are more reliably estimated.

For the red and blue ambiguous first-level categories associated with pattern (b) in Fig. 6, the reverse classification is implemented in a similar manner to partition the samples according to the u -, v -, and o_{uv} -axes. The main difference is that the demosaicing equations represented similarly to (9) are written by following the derivative correlation model in (8), where $\mathbf{s}_n^{(t)}$ contains the supporting derivatives computed from both the RAW image and the green plane.

This EMRC algorithm can be extended to the cases where a first-level category needs to be more thoroughly divided, i.e., when more than three subcategories are needed. Such a scenario is necessary when the regularity of complex demosaicing algorithms needs to be thoroughly investigated.

For patterns (c) and (d) in Fig. 6, the demosaicing axes are clear as the nearest two sensor samples are either vertically or horizontally arranged. Such first-level categories are directly exported to the second level and the corresponding demosaicing weights are computed similarly to the maximization step of the above EMRC algorithm.

B. Computation of Demosaicing Features

With the optimal weights determined for the 16 demosaicing categories, we compute three types of features below.

Weights: These features represent the applied demosaicing formulas with a total of 312 weights computed for the 16 demosaicing categories.

Error Statistics: With the optimal weights \mathbf{w} available, the absolute errors are given as

$$|e| = |\mathbf{Q}\mathbf{w} - \mathbf{z}| \quad (14)$$

where \mathbf{Q} is the matrix of supporting derivatives and \mathbf{z} is the vector of the corresponding derivatives. For each category, we compute four error cumulants, including the mean, variance, skewness, and kurtosis. For 16 categories, a total of 64 error cumulants are computed, which statistically reveal the goodness that our estimated weights fit the underlying demosaicing algorithm.

Normalized Group Sizes: After partitioning an ambiguous first-level category using the EMRC algorithm, the percentage of the demosaiced samples distributed to the three subcategories is a good indicator of the implicit grouping adopted by the underlying demosaicing algorithm. The normalized sizes of the subcategories in percentages are also included as our features. For a total of four ambiguous first-level categories, we compute eight such features.

In commercial digital still cameras, the four versions of Bayer CFAs in Fig. 1(b) are most likely adopted equally. Hence, we apply our detection method four times to cater to the four possibilities. Consequently, we obtain $312 \times 4 = 1248$ weights, $64 \times 4 = 256$ error cumulants, and $8 \times 4 = 32$ normalized group sizes. Though the feature dimension increases fourfold, there are some key advantages.

- 1) Detection of the correct Bayer CFA is not needed, and the discriminative CFA information is automatically included in the overall feature set.
- 2) The correct Bayer CFA must be present if Bayer CFA is used. We find the features computed based on the three incorrect Bayer CFAs also provide useful relative information, and the four channels of demosaicing features statistically form stable and unique patterns.
- 3) Other non-Bayer CFAs in Fig. 1(b) share common properties with Bayer CFAs, including 2×2 periodicity and mosaic lattice, which make our derivative correlation models still applicable to such CFAs. Demosaicing based on these CFAs will also cause stable and unique imbalance pattern among these four channels of statistical features, and our demosaicing features based on four Bayer CFAs help comprehensively represent this statistical imbalance.

The proposed total 1536 features comprehensively represent the demosaicing regularity of all 16 demosaicing categories. The overall feature computational time averaged over 100 runs on a P4-2.66 GHz PC with MATLAB 7.4 for 100 different color images of sizes 512×512 is about 45 s.

In view of the high dimensionality, which requires huge training data and causes slow classifier training and forensic response, we reduce the feature dimension by selecting a compact subset of features using sequential forward floating search (SFFS) algorithm [29]. Starting from an empty feature set, the SFFS algorithm performs stepwise feature inclusion and conditional feature removal to select a subset of features. Compared with simple sequential searching algorithms, the backtracking mechanism employed by SFFS allows removing the previously selected but currently useless features due to inclusion of new features, which more likely result in an optimal feature subset.

V. SIMULATION RESULTS AND DISCUSSION

In our experiment, we select 16 conventional demosaicing algorithms in Table I. Note these algorithms are highly diversified, including the early nonadaptive algorithms as well as the state-of-art highly adaptive algorithms. We have also included two pairs of close demosaicing algorithms, i.e., Chang's and Wang's methods are extensions of Pei's and Kimmel's proposals, respectively. One can refer to [27] and [28] for details about the 16 methods used.

A. Reestimation Accuracy

Our derived demosaicing weights together with (4) can be used to reestimate the demosaicing samples from the sensor samples. The reestimation accuracy reveals the preciseness with which our estimated weights match the formulas used by the underlying demosaicing algorithm.

In this experiment, we compare our reestimation accuracies for the 16 demosaicing algorithms in Table I with the detection algorithm [7] based on syntactic images. The syntactic set contains 1000 color images of 512×512 , which are cropped from the center of 1000 photos taken with different cameras and then downsampled sufficiently to remove previous filtering characteristics. We first sample the RAWs from these images according to the first Bayer CFA in Fig. 1(b) and then separately demosaic these RAWs with the 16 demosaicing algorithms. Our proposed detection model is then applied to compute both the optimal weights and the corresponding errors for green channel of

TABLE I
COMPARISON OF 16 CONVENTIONAL DEMOSAICING ALGORITHMS

ID	Algorithm	Edge Adaptiveness	Domain (Refinement)	Reconstructive Filter (Size)
1	Bilinear	Non-adaptive	Intra-channel	Fixed (3×3)
2	Bicubic	Non-adaptive	Intra-channel	Fixed (7×7)
3	Cok 86	Adaptive	Intra-channel	Mixed (≥3×3)
4	Cok 87	Non-adaptive	Color hue	Fixed (3×3)
5	Freeman 88	Non-adaptive	Color diff.	Median (3×3)
6	Laroche 94	Adaptive	Mixed	Fixed (3×3)
7	Hamilton 97	Adaptive	Color diff.	Fixed (3×3)
8	Kimmel 99	Adaptive	Color hue (Inverse diffusion)	Adaptive (3×3)
9	Li 01	Non-adaptive	Color diff.	Adaptive
10	Gunturk 02	Non-adaptive	Color diff. (Iterative)	Fixed (5×5)
11	Pei 03	Adaptive	Color diff. (Iterative)	Adaptive (3×3)
12	Wu 04	Adaptive	Color diff. (Iterative)	Fixed (3×3)
13	Chang 04	Adaptive	Color diff. (Iterative)	Adaptive (5×5)
14	Wang 05	Adaptive	Color diff. (Iterative)	Adaptive (3×3)
15	Hirokawa 05	Adaptive	Color diff. (Iterative)	Median (5×5)
16	Alleysson 05	Non-adaptive	Chrominance	Fixed (11×11)

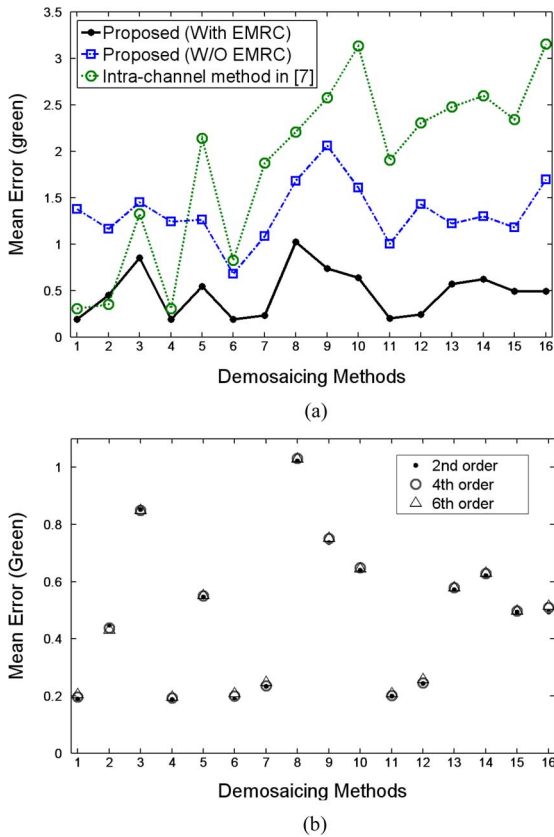


Fig. 7. Comparison of mean absolute reestimation errors for 16 demosaicing methods based on (a) different detection algorithms and (b) the proposed algorithm with different approximation orders. Refer to Table I for IDs of the demosaicing methods. The mean absolute error is computed when each color sample is represented by 8 bits, i.e., from zero to 255.

each demosaiced image. Based on the same rough reverse classification in [7], our results in Fig. 7(a) show that the derivative-based correlation model in (6) is more accurate for most adaptive demosaicing methods that utilize cross-channel information to demosaic the green channel. If the proposed EMRC is applied, the mean absolute errors drop to a very low level for all 16 demosaicing algorithms. The comparison results suggest that

our method achieves large margins of improvement on accuracies especially for the adaptive demosaicing methods, where the reconstruction is in cross-channel domains. Fig. 7(b) suggests that the second-, fourth-, and sixth-order approximations give similar mean errors. In Fig. 8, we can see the iterations in the proposed EMRC algorithm monotonically reduce the average reestimation error to a low level for two very different demosaicing methods. This demonstrates that our proposed EMRC algorithm efficiently improves the detection accuracy for diversified demosaicing algorithms.

B. Classification of Demosaicing Algorithms

In this experiment, we classify the 16 demosaicing algorithms using our proposed demosaicing features. Since demosaicing is not the last process in the camera processing pipeline, our experiment also takes into account that common camera postdemosaicing processes including quantization (QT), white balancing (WB), edge enhancement (EE), gamma correction (GC), color space transformation (CST), and lossy JPEG compression. We also include adding zero-mean additive white Gaussian noise (AWGN) as one general form of distortion. The syntactic image set for this experiment is the same as the previous experiment. After demosaicing the 1000 images with these 16 algorithms, the demosaiced images further go through the above postprocessing separately. Out of the 1000 syntactic images, 600 images per demosaicing algorithm and per distortion process are randomly selected for training and the rest for testing.

After performing feature extraction, we follow the LIBSVM guild [21] to train two probabilistic support vector machine (PSVM) classifiers with radial basis function kernel. For the six postprocesses excluding JPEG, we use 57 600 training and 38 400 testing images. For JPEG of seven different quality factors, we use 67 200 training and 44 800 testing images. Compared with the conventional SVM, PSVM also studies distribution of SVM outputs and maps them into probability scores by optimizing a sigmoid function [22], [23]. Based on the same setup, the comparison results in Fig. 9(a) demonstrate that our 200 demosaicing features selected by SFFS result in an average of 2.9% error rate for postdemosaicing processes including QT, WB, EE, GC, CST, and AWGN, which reduce the error rates of 10.1% for the derived weights in [7] (441 features) by 2.5 times. With only 24 features selected, our average error rate increases to 9.1%, which is still 3.9 times smaller than 44.8%, the average error rate for the EM weights [3], [4] (24 features). We attribute the significant error rate reduction to our accurate detection model, which more comprehensively captures the differences between the close demosaicing methods, and our features contain less content-dependent variations. Our good performance also suggests the uniqueness of demosaicing regularities is still largely preserved after the six common postdemosaicing distortion processes.

For lossy JPEG compression, the test accuracies in Fig. 9(b) monotonically decrease as the JPEG quality decreases. As expected, a low JPEG quality factor implies large quantization step sizes, especially for the high-frequency discrete cosine transform components. While demosaicing regularity contains rich high-frequency correspondence among neighboring color samples, low-quality JPEG compression can remove the uniqueness of detected demosaicing regularity. Though JPEG compression could significantly deteriorate the classification performance,

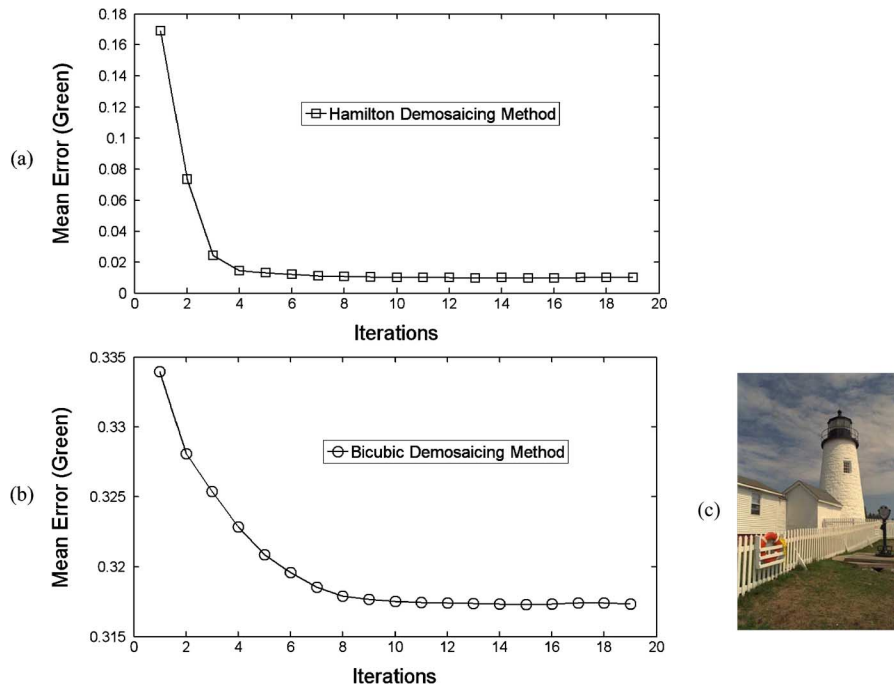


Fig. 8. Mean absolute prediction error versus iterations for (a) an adaptive (Hamilton) and (b) a nonadaptive (bicubic) demosaicing method. (c) Test image.

at a typical JPEG quality of 80, our 83% top-1 test accuracy based on 200 selected features still suggests a reliable identification performance, especially when multiple pairs of close demosaicing algorithms are present. The comparison results show that our average error rate of 28% based on 200 selected features is 17.6% lower than 34%, the average error rate for the derived weights in [7]. With the same number of features, our test accuracy based on 24 features confidently outperforms that of the 24 EM weights in [3] and [4].

C. Classification of Postprocesses

Different types of postdemosaicing processes distort the demosaicing regularity in unique manners. In this experiment, with the demosaicing algorithm fixed as Hamilton's method [26], we classify seven postdemosaicing processes including quantization (8-bit), WB, EE (PSNR = 30 dB using unsharp mask), GC ($1/\gamma = 1/2.2$), CST (from CIEXYZ to sRGB), AWGN (30 dB), and lossy JPEG compression (Q-factor = 80) using the proposed features. With 600 randomly selected training images and 400 test images per distortion process, i.e., 4200 training and 2800 testing images in total for the seven distortions, we achieve a test classification accuracy of 97.3% using a similar PSVM classifier based on only five selected features. This high classification rate shows our proposed features also effectively capture the unique distortion characteristics of the different postdemosaicing processes. Since the postprocessing in commercial DSCs can differ significantly in the type of inclusive processes, their sequence, and the parameters, our good performance implies that the proposed features also can be used as a fingerprint of the postdemosaicing processing.

D. Sensitivity to Image Variations

Rich content variations in RAW samples make detection of the demosaicing regularity easier. In this simulation, we consider the extreme case of uniform scenery, and the only image

variations are contributed by sensor imperfections aggregated from sensor noises, dust, and process distortions. We assume these noises are AWGN, and the required noise level for reliable identification of the 16 demosaicing algorithms based on our proposed features is studied.

We first create a noisy image set containing 1200 images by adding eight levels (PSNR = 10, 20, ..., 80 dB) of random AWGN noises to the uniform "sky" scenery in Fig. 10(a). These noisy images are then separately demosaiced with the 16 algorithms. With a similar PSVM classifier and by selecting only 50 proposed features using SFFS, our comparison result in Fig. 11 shows, for a cutoff level of 90%, our required PSNR is 66 dB, which is about 14 dB higher than [7]. This suggests our proposed features require significantly fewer scenery variations to achieve good identification of source demosaicing algorithms.

VI. FORENSIC APPLICATIONS

A. Camera Model Identification

The real camera processing pipelines in commercial DSCs contain proprietary knowledge. In this section, we further test the proposed demosaicing features in distinguishing 14 commercial DSC cameras in Table II. We first establish a photo dataset consisting of 200 photos per camera. All these photos are direct outputs from their cameras and are stored in the default JPEG formats. As illustrated in Fig. 12(a), we crop 12 nonoverlapped image blocks from each selected photo at 12 fixed locations to create 2400 image blocks per camera, with some samples shown in Fig. 12(b). For each camera, we further divide the image blocks into a training set of 1584 blocks cropped from 132 randomly selected photos and a test set of the remaining image blocks. For 14 cameras, the number of blocks used for training and testing is, respectively, 22 176 and 11 424.

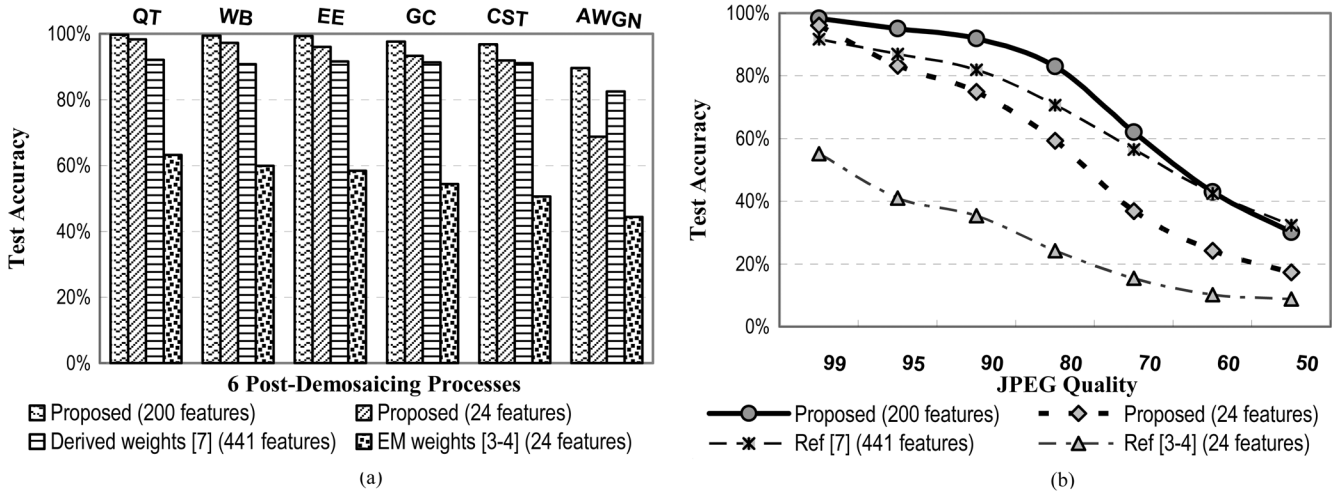


Fig. 9. Comparison of source demosaicing algorithm identification using various demosaicing features with presence of (a) six common postdemosaicing processes and (b) lossy JPEG compression of various quality factors. In (a), the postprocesses are **QT**: quantizing color samples of the demosaiced image to $\{0, 1, \dots, 255\}$; **WB**: white balancing with 3×3 transformation matrix $\mathbf{T} = [.85, .07, .08; .01, .88, .11; .03, .08, .89]$; **EE**: edge enhancement using unsharp mask (PSNR = 30 dB); **GC**: gamma correction with $1/\gamma = 1/2.2$; **CST**: color space transformation from CIEXYZ to SRGB; **AWGN**: zero-mean white Gaussian random noise (PSNR = 30 dB).

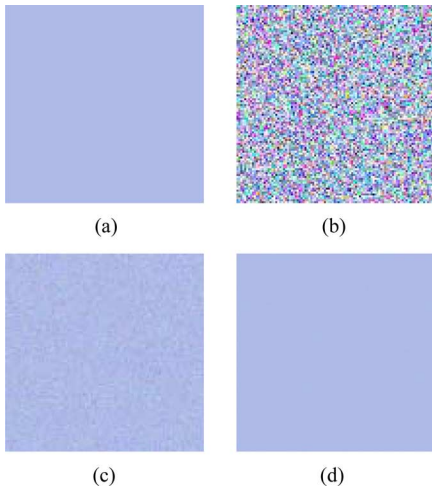


Fig. 10. (a) A uniform “sky” scenery (256 × 256) and after adding AWGN camera sensor noises of PSNR (b) = 10 dB; (c) = 30 dB, and (d) = 50 dB.

TABLE II
CAMERA MODELS USED

ID	Camera model
1	Canon Ixus i
2	Canon Powershot A620
3	Canon EOS 400D
4	Canon EOS 10D
5	Nikon Coolpix S210
6	Nikon D70
7	Lumix DMC-FX01
8	Lumix DMC-FX2
9	Olympus U300d
10	Olympus E-500
11	Sony Cybershot DSC-P73
12	Sony Alpha DSLR A350
13	Casio EX-Z60
14	Fujifilm FinePix Z2

With a similar PSVM classifier, our identification results based on 250 selected features by SFFS in Table III demonstrate an excellent performance with an average test accuracy

of 97.5%. Since the result is achieved based on individual blocks, the accuracy can be further improved to close to 100% simply by averaging the probabilistic scores of all 12 image blocks cropped from a test photo. The cameras we have tested include multiple models from a same camera manufacturer, e.g., four Canon models and two models each from Nikon, Lumix, Olympus, and Sony. Our results in Table III show the camera models from different manufacturers can be distinguished almost as accurately as the camera models from the same manufacturers.

With a close examination on the wrongly classified camera blocks, we found that the 2.5% total classification errors are mainly contributed by some low-quality blocks, and we manually classify them into five categories, as illustrated in Fig. 13. About 49.5% of the total errors are contributed by the “saturated” and “uniform” categories. Images in these two categories lack content variations, which makes reliable detection almost impossible. The “chromatic” and the “structured” categories also contribute a small portion of errors because these images lack either color variations or edge-type variations, which makes comprehensive detection of demosaicing regularity difficult. Though the majority of the low-quality test blocks are still correctly classified, our finding suggests that the error rate can be further reduced if we wisely crop the image blocks at locations where rich color and edge information are present.

B. RAW-Tool Identification

Digital single-lens reflex cameras usually allow the sensor samples to be saved into RAW formats, which can be developed into photos using RAW tools at a later time. Similar to the camera processing, these tools demosaic the RAWs and then apply some postdemosaicing processes. However, since these RAW tools are designed for PCs, common constraints such as processor speed, memory size, and shot-to-shot delay are no longer among the key design considerations. Hence, these RAW tools are affordable to implement more complex demosaicing and postprocessing to achieve higher image quality. In this test, we classify ten commercial RAW tools in Table IV with our proposed features.

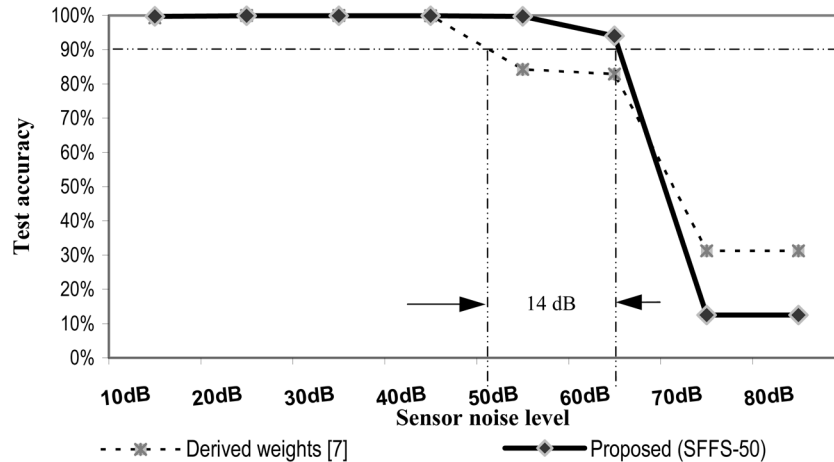


Fig. 11. Comparison of test accuracies in classification of 16 demosaicing algorithms based on uniform blocks with various sensor noise levels.

TABLE III
CONFUSION MATRIX (%) FOR 14-CAMERA CLASSIFICATION (250 FEATURES), WHERE EMPTY FIELDS INDICATE ZEROS

Ave. rate = 97.5%	Predicted camera													
	1	2	3	4	5	6	7	8	9	10	11	12	13	14
1	96.1	1.3	0.1	0.1		2.0		0.4						
2	1.1	90.1	1.3			6.5	0.1	0.5						
3	0.2		98.5	0.5		0.1	0.1				0.4	0.2		
4	Canon			100	Nikon									
5	0.1		0.4	0.5	98.0	0.1			0.2	0.1				0.6
6	1.6	2.3		0.6	1.6	93.3	0.1	Lumix	0.3	0.1				0.1
7			0.4		0.1		97.8		1.2	0.2		0.3		
8	0.3	0.1	0.8	0.3	0.6		97.8							0.1
9					0.6	0.1			99.3					
10						0.1	Olympus	0.1	99.4			0.4		
11			0.1	0.1	0.6	0.3				Sony	98.8	0.1		
12					0.1	0.1	0.2	0.3		0.5		98.8		
13						0.2			0.3				Casio	99.5
14	0.1	0.1			0.5	1.1			0.1				Fujifilm	98.0

We first develop 200 RAWs (captured by an Olympus E-500 camera) into uncompressed TIFF photos using the ten commercial RAW tools in Table IV. Based on a similar setup as the camera identification experiment, we use a total of 15 840 cropped image blocks for training and 8160 blocks for testing. We identify the source RAW tool using only 50 selected features based on image blocks. Our average identification accuracy of 99.1% in Table V shows that the proposed detection framework can efficiently capture the unique processing characteristics of these RAW tools.

C. Analysis on Features Selected

Considering that the selected features largely depend on both the datasets used and the SFFS configurations, we show in Table VI the more reliable distribution of the selected features. Among the three different types of demosaicing features, we find that for both camera and RAW-tool identifications, a dominant percentage of about 80% selected features are the weight features followed by the error statistics features, and the least are the normalized group size features. Though partially due to the different population sizes of different feature types, these results also suggest that our estimated weights contain the richest discriminant information. The contribution to the selected feature set from the 16 demosaicing categories is rather even. We also note that 36% of selected features are

TABLE IV
RAW TOOLS USED

ID	RAW tool
1	ACDSee v10
2	Breeze Browser Pro v1.7
3	Capture One v3.7.8
4	Olympus Master v2
5	Photoshop CS2
6	Picture Window Pro v4.0
7	Rawshooter Essential 2006
8	Silkypix Developer Studio v3.0
9	StepOK v1.1
10	Corel Paintshop Pro 12

contributed from the green demosaicing categories for camera model identification and only 20% for the RAW-tool identification. Considering the major difference is that all camera photos in our experiment are in JPEG format and the converted RAW photos are in TIFF format, the difference in contribution percentages from the green categories is likely caused by JPEG compression. In the TIFF photos, we observe in many cases that our detected demosaicing regularity from the different green categories tends to be more similar, exhibiting less diversity information. Hence, fewer features are selected from the green categories.

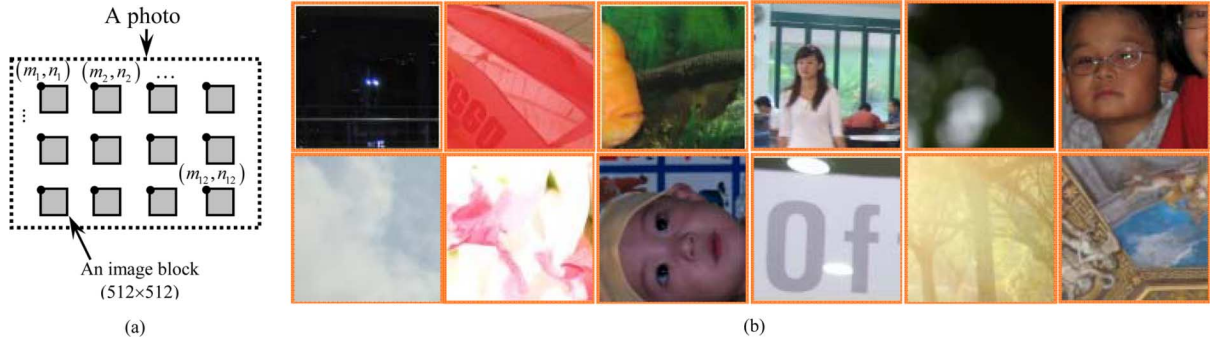


Fig. 12. Image set creation for camera identification. (a) Schematic diagram of cropping blocks from a photo, where black dots indicate the top-left corners $\{m, n\}$ of the blocks, which are set to be odd number to avoid shifts to underlying CFA. (b) Samples of cropped image blocks.

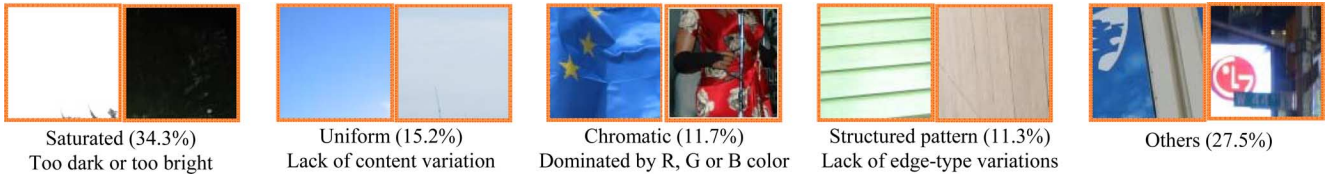


Fig. 13. Samples of wrongly classified camera image blocks.

TABLE V
CONFUSION MATRIX (%) FOR TEN-RAW-TOOL CLASSIFICATION (50 FEATURES), WHERE EMPTY FIELDS INDICATE ZEROS

Ave. rate = 99.1%	Predicted RAW tool										
	1	2	3	4	5	6	7	8	9	10	
Input RAW tool	1	98.5	0.1	0.1		0.1		0.2		1.0	
	2		99.9						0.1		
	3			98.4	0.4		0.1		1.0	0.1	
	4				100						
	5	0.4		0.1		98.4		0.2	0.3	0.6	
	6	0.1					97.8		0.1	2.0	
	7				0.1	1.3		98.6			
	8	0.1			0.1	0.1	0.1		99.6		
	9						0.1			99.8	0.1
	10						0.1		0.1	0.2	99.6

TABLE VI
CONTRIBUTION PERCENTAGES (%) TO THE SFFS SELECTED FEATURES FROM THREE DIFFERENT FEATURE TYPES [WEIGHTS (WT), ERROR STATISTICS (ES), NORMALIZED GROUP SIZES (NGS)] AND FROM 16 DIFFERENT DEMOSAICING CATEGORIES (REFER TO FIG. 5 FOR THE DEMOSAICING CATEGORIES)

Identification application	Feature type			Demosaicing category															
	WT	ES	NGS	G on r			G on b			R on g		R on b		B on g		B on r			
				x	y	o_{xy}	x	y	o_{xy}	x	y	u	v	o_{uv}	x	y	u	v	o_{uv}
Camera models	83	14	3	5	7	9	4	6	5	5	5	7	9	6	5	5	7	7	8
RAW tools	76	24	0	6	2	6	0	4	2	8	4	12	10	4	6	12	6	8	10

VII. CONCLUSION

In this paper, we present an accurate detection framework of image demosaicing regularity. Our proposed method addresses the common differences of color filtering and demosaicing algorithms, and the accurate detection is achieved by a precise reverse classification together with partial derivative correlation models. In the reverse classification, an EMRC algorithm is demonstrated to be effective in resolving the ambiguous demosaiced axes. Through using partial derivative correlation models, our method efficiently detects both the cross- and the intrachannel correlation caused by demosaicing. By significantly reducing our feature dimension using sequential forward floating search, the simulation results show that our proposed demosaicing features confidently outperform two existing demosaicing detection methods in identifying 16 demosaicing

algorithms in the presence of various common postdemosaicing processes. Our proposed features are also highly effective in distinguishing different postprocesses and are more sensitive to small scenery variations. When applied to real forensic applications, our reduced sets of demosaicing features achieve nearly perfect average test identification accuracies of 97.5% for 14 commercial DSCs of different models and 99.1% for 10 RAW-tools based on large number of cropped image blocks, which contain a mixture of good and bad quality images.

Complementing the current proposed approach to identify different image software processing pipelines, additional features such as sensor noise pattern [20] are needed in identification of individual cameras of the same model. Further investigation effort also includes verifying the effectiveness of our proposed demosaicing features on the camera models of non-Bayer CFAs.

ACKNOWLEDGMENT

The authors would like to thank Prof. P. Xue and Dr. L. Chang for kindly sharing source codes of the demosaicing algorithms used in this paper.

REFERENCES

- [1] D. Cyranoski, "Verdict: Hwang's human stem cells were all fakes," *Nature*, vol. 439, pp. 122–123, 2006.
- [2] H. Pearson, "Forensic software traces tweaks to images," *Nature*, vol. 439, pp. 520–521, 2006.
- [3] A. C. Popescu and H. Farid, "Exposing digital forgeries in color filter array interpolated images," *IEEE Trans. Signal Process.*, vol. 53, no. 10, pp. 3948–3959, Oct. 2005.
- [4] S. Bayram, H. T. Sencar, N. Memon, and I. Avciabas, "Source camera identification based on CFA interpolation," in *Proc. ICIP*, 2005, vol. 3, pp. III-69–III-72.
- [5] S. Bayram, H. T. Sencar, and N. Memon, "Improvements on source camera-model identification based on CFA interpolation," in *Proc. IFIP WG 11.9 Int. Conf. Digital Forensics*, Orlando, FL, 2006, pp. 24–27.
- [6] Y. Long and Y. Huang, "Image based source camera identification using demosaicing," in *Proc. MSP*, 2006, pp. 419–424.
- [7] A. Swaminathan, M. Wu, and K. J. R. Liu, "Nonintrusive component forensics of visual sensors using output images," *IEEE Trans. Inf. Forensics Security*, vol. 2, no. 1, pp. 91–106, Mar. 2007.
- [8] I. Avciabas, N. Memon, and B. Sankur, "Steganalysis using image quality metrics," *IEEE Trans. Image Process.*, vol. 12, no. 2, pp. 221–229, Feb. 2003.
- [9] J. Fridrich, D. Soukal, and J. Lukáš, "Detection of copy-move forgery in digital images," in *Proc. Digital Forensic Research Workshop*, Cleveland, OH, Aug. 2003, pp. 55–61.
- [10] K. S. Choi, E. Y. Lam, and K. K. Y. Wong, "Source camera identification using footprints from lens aberration," *Proc. SPIE*, vol. 6069, pp. 155–162, 2006.
- [11] J. Lucas, J. Fridrich, and M. Goljan, "Digital camera identification from sensor pattern noise," *IEEE Trans. Inf. Forensics Security*, vol. 1, no. 2, pp. 205–214, Jun. 2006.
- [12] S. Lyu and H. Farid, "Steganalysis using higher-order image statistics," *IEEE Trans. Inf. Forensics Security*, vol. 1, no. 1, pp. 111–119, Mar. 2006.
- [13] S.-F. Chang, "Blind passive media forensics: Motivation and opportunity," in *Proc. MCAM*, 2007, pp. 57–59.
- [14] O. Celiktutan, B. Sankur, and I. Avciabas, "Blind identification of source cell-phone model," *IEEE Trans. Inf. Forensics Security*, vol. 3, no. 3, pp. 553–566, Sep. 2008.
- [15] A. E. Dirik, H. T. Sencar, and N. Memon, "Digital single lens reflex camera identification from traces of sensor dust," *IEEE Trans. Inf. Forensics Security*, vol. 3, no. 3, pp. 539–552, Sep. 2008.
- [16] T.-T. Ng, S.-F. Chang, and M.-P. Tsui, "Using geometry invariants for camera response function estimation," in *Proc. CVPR*, 2007, pp. 1–8.
- [17] M. Chen, J. Fridrich, M. Goljan, and J. Lucas, "Determining image origin and integrity using sensor noise," *IEEE Trans. Inf. Forensics Security*, vol. 3, no. 1, pp. 74–89, Mar. 2008.
- [18] A. Swaminathan, M. Wu, and K. J. Ray Liu, "Digital image forensics via intrinsic fingerprints," *IEEE Trans. Inf. Forensics Security*, vol. 3, no. 1, pp. 101–117, Mar. 2008.
- [19] A. Swaminathan, M. Wu, and K. J. Ray Liu, "Component forensics," *IEEE Signal Process. Mag.*, vol. 26, no. 2, pp. 38–48, Mar. 2009.
- [20] J. Fridrich, "Digital image forensics," *IEEE Signal Process. Mag.*, vol. 26, no. 2, pp. 26–37, Mar. 2009.
- [21] C.-W. Hsu, C.-C. Chang, and C.-J. Lin, "A practical guide to support vector classification 2008 [Online]. Available: <http://www.csie.ntu.edu.tw/~cjlin/libsvm>
- [22] J. Platt, "Probabilistic outputs for support vector machines and comparison to regularized likelihood methods," in *Advances in Large Margin Classifiers (Neural Information Processing)*. Cambridge, MA: MIT Press, 2000, pp. 61–74.
- [23] T.-F. Wu, C.-J. Lin, and R. C. Weng, "Probability estimates for multi-class classification by pairwise coupling," *J. Machine Learn. Res.*, vol. 5, pp. 975–1005, 2004.
- [24] P. C. Hansen, *Rank-Deficient and Discrete Ill-Posed Problems*. Philadelphia, PA: SIAM, 1998.
- [25] R. Ramanath, W. E. Snyder, Y. Yoo, and M. S. Drew, "Color image processing pipeline," *IEEE Signal Process. Mag.*, vol. 22, no. 1, pp. 34–43, Jan. 2005.
- [26] J. F. Hamilton Jr. and J. E. Adams, "Adaptive Color Plane Interpolation in Single-Sensor Color Electronic Camera," U.S. Patent 5 629 734, 1997.
- [27] J. Adams, "Interaction between color plane interpolation and other image processing functions in electronic photography," *Proc. SPIE*, vol. 2416, pp. 144–151, 1995.
- [28] X. Li, B. Gunturk, and L. Zhang, "Image demosaicing: A systematic survey," *Proc. SPIE*, vol. 6822, pp. 68221J–68221J-15, 2008.
- [29] P. Pudil, F. J. Ferri, J. Novovicov, and J. Kittler, "Floating search methods for feature selection with non-monotonic criterion function," in *Proc. Int. Conf. Pattern Recognit.*, 1994, vol. 2, pp. 279–283.



Hong Cao (S'08) received the B.Eng. and M.Eng. degrees (with first-class honors) in electrical and electronic engineering from Nanyang Technological University (NTU), Singapore, in 2001 and 2003, respectively, where he is currently pursuing the Ph.D. degree at the School of Electrical and Electronic Engineering.

He has been a Software Developer for several years, mainly working on electronic writing-related software products. Since 2007, he has been a Research Associate with the School of Electrical and Electronic Engineering, NTU. His current research interests include multimedia forensics, data hiding and document authentication, bilevel image steganalysis, and pattern classification.



Alex C. Kot (S'85–M'89–SM'98–F'06) has been with Nanyang Technological University (NTU), Singapore, since 1991. He was Head of the Division of Information Engineering, School of Electrical and Electronic Engineering, NTU, for eight years and Associate Chair for Research and Vice Dean for Research there. He is currently a Professor and Associate Dean of the College of Engineering. He has published extensively in the areas of signal processing for communication, biometrics, image forensics, and information security. He was an Associate Editor of the *EURASIP Journal of Advanced Signal Processing*.

Dr. Kot is a Fellow of IES. He was an Associate Editor of the *IEEE TRANSACTIONS ON SIGNAL PROCESSING*, *IEEE TRANSACTIONS ON CIRCUITS AND SYSTEMS FOR VIDEO TECHNOLOGY*, and *IEEE TRANSACTIONS ON CIRCUITS AND SYSTEMS—PART I: REGULAR PAPERS* and *PART II: ANALOG AND DIGITAL SIGNAL PROCESSING*. He was a Guest Editor for two *IEEE JOURNALS*. He is currently an Associate Editor of the *IEEE TRANSACTIONS ON MULTIMEDIA* and *IEEE SIGNAL PROCESSING LETTERS* and an Editorial Board Member of *IEEE SIGNAL PROCESSING MAGAZINE*. He is a member of the Visual Signal Processing and Communication Technical Committee and the Image and Multidimensional Signal Processing Technical Committee. He has served the IEEE in various capacities, including General Cochair for the 2004 IEEE International Conference on Image Processing. He was an IEEE Distinguished Lecturer.